EDGE ARTICLE

Check for updates

Zirconium metal–organic frameworks incorporating tetrathiafulvalene linkers: robust and redox-active matrices for *in situ* confinement of metal nanoparticles†

Jian Su, [ID] ‡[a] Shuai Yuan, [ID] ‡[b] Tao Wang,[a] Christina Tori Lollar,[b] Jing-Lin Zuo, [ID] *[a] Jiangwei Zhang [ID] *[c] and Hong-Cai Zhou [ID] *[b]

Redox-active metal–organic frameworks (MOFs), with highly ordered porous structures and redox tunability, have attracted research interest in the fields of catalysis, energy storage, and electrochemical sensing. However, the chemical lability has limited the application scope of many redox-active MOFs. Herein, we selected stable Zr_6 inorganic nodes and redox-active tetrathiafulvalene (TTF)-based linkers to construct two robust, redox-active MOFs, namely compounds 1 ($[Zr_6(TTFTB)_2O_8(OH_2)_8]$) and 2 ($[Zr_6(Me-TTFTB)_{1.5}O_4(OH)_4(C_6H_5COO)_6]$) (TTFTB = tetrathiafulvalene tetrabenzoate; Me-TTFTB = tetrathiafulvalene tetramethylbenzoate). The structure and topology of the MOFs were controlled by tuning the linker conformation through steric effects, resulting in a variety of pore structures from microporous channels (compound 1) to hierarchically micro/mesoporous cages (compound 2). Compound 2 shows high porosity with a BET surface area of 1932 m^2 g^{-1} and strong chemical stability in aqueous solutions with pH ranging from 1 to 12. Furthermore, the reductive TTF moieties allow for *in situ* generation and stabilization of ultra-small noble metal (Ag, Pd, and Au) nanoparticles by incubating MOFs in the respective metal salt solution. Single crystal structures, TEM images, and pore size distribution data from N_2 adsorption measurements indicated that the metal nanoparticles were mostly placed in the small cubic cavities of hierarchically porous compound 2, leaving the large cages open for substrate diffusion. As a proof of concept, Pd NPs@compound 2 was utilized as a heterogeneous catalyst for aerobic oxidation of alcohols, showing noteworthy activity and recyclability.

Introduction

Metal–organic frameworks (MOFs) are crystalline porous materials constructed from metal ions/clusters and organic linkers showing high surface areas and tunable pore environments. They have attracted considerable research interest in the fields of gas storage,[1,2] separations,[2,3] energy storage,[4] catalysis[5] and chemical sensing.[6] While many MOFs remain inert under application conditions, recent studies have highlighted their redox activity potential arising from metal ions,[7–15] organic

[a]*State Key Laboratory of Coordination Chemistry, School of Chemistry and Chemical Engineering, Collaborative Innovation Center of Advanced Microstructures, Nanjing University, Nanjing 210093, P. R. China. E-mail: zuojl@nju.edu.cn*

[b]*Department of Chemistry, College Station, TX 77843, USA. E-mail: zhou@chem.tamu.edu*

[c]*State Key Laboratory of Catalysis, Dalian Institute of Chemical Physics, Chinese Academy of Sciences (CAS), Dalian 116023, China. E-mail: jwzhang@dicp.ac.cn*

† Electronic supplementary information (ESI) available. CCDC 1850014–1850018 1974366. For ESI and crystallographic data in CIF or other electronic format see DOI: 10.1039/c9sc06009j

‡ These authors contributed equally to this work.

linkers,[16–25] or the guest molecules.[18,26] Redox-active MOFs represent a unique class of switchable solid materials in which the different redox states with distinct physical properties can be achieved by redox modulation.[27] This will expand the application of MOFs to exciting new areas including gas adsorption,[28,29] microporous conducting materials,[7,16,17] catalysis,[30] magnetism,[31–33] energy storage,[34–36] and electrochemical sensing.[37] For example, Long and coworkers reported a redox-active MOF, $Fe_2(BDP)_3$ (BDP = 1,4-benzenedipyrazolate), displaying a nearly 10 000-fold enhancement in conductivity upon reduction by potassium naphthalenide.[7] Yoshikawa, Awaga and coworkers studied the electrochemistry of Cu(2,7-anthraquinone dicarboxylate) in lithium batteries and revealed the coexistence of metal and linker redox activities within the MOF.[38] Studies on redox-active MOFs not only provide new insights into charge transfer mechanisms but also highlight potential applicability in electrochemical devices.

Tetrathiafulvalene (TTF) and its derivatives have been widely investigated as important electron donor components for photo-thermal conversion,[39] supramolecular switching,[40] solid catalysis,[30] magnetic materials,[33] and conductive materials.[41–45]

TTF motif has also been adopted as a linker fragment in the synthesis of redox-active MOFs with intriguing conductivity[16,17,40,46–49] and redox switchable adsorption properties.[28,29] The highly electron donating nature of the TTF moiety makes TTF-based MOFs highly reductive. Indeed, the redox potential of TTF is lower than most noble metal cations including Ag^+, Au^{3+}, Pt^{2+}, Pd^{2+}, Ru^{3+}, Ir^{3+}, *etc.* Therefore, we propose that TTF-based MOFs can act as suitable matrices to generate metal nanoparticles (MNPs) *in situ* from metal cation solutions and stabilize them from aggregation by pore confinement.

Usually, MNPs are immobilized into MOFs following a two-step process involving the intrusion of metal cation precursors followed by treatment with reducing reagents (such as $NaBH_4$ or H_2) to form MNPs.[50–53] Compared with redox-inert MOFs, redox-active TTF-based MOFs allows for *in situ* reduction of metal cation precursors by the framework. This will favor the formation of well-dispersed, ultra-small metal nanoparticles by avoid inhomogeneity of reducing reagents. In fact, the idea of generating nanoparticles in redox-active MOFs has been demonstrated by Suh and coworkers using a redox-active macrocyclic nickel(II)-based MOF or organic redox centers MOF (triphenylamine-based linker) as a matrix to produce and stabilize MNPs without external reducing agent.[8,10,14,15,54] Despite these initial works, the application of MNPs@MOF materials in catalysis are often hindered by their poor chemical stability. To address these problems, we selected stable Zr_6 inorganic nodes and TTF-based linkers to construct robust and redox-active MOFs. Two TTF-based linkers with the same connectivity but different conformations were selected, giving rise to two MOFs with different pore architectures (compounds **1** and **2**). Taking advantage of the reductive TTF moieties, ultra-small noble metal (Ag, Pd, and Au) nanoparticles were generated *in situ* and stabilized in the cavities of compounds **1** and **2** by incubating the MOFs in solutions of the respective metal salts. With highly accessible metal nanoparticles in the hierarchically porous framework, Pd NPs@**2** was utilized as a heterogeneous catalyst for aerobic oxidation of alcohols.

Results and discussion

Controlling pore architecture by steric tuning of linkers

Current Zr-tetracarboxylate-based MOFs in the literature provide a blueprint for the design of our MOF system.[55] Topologically, TTF-based linkers, such as tetrathiafulvalene tetrabenzoate (TTFTB),[16,17,29,30,46,47,49] can be simplified into 4-connected square planar nodes, whereas Zr_6 clusters have variable connection numbers and can act as 12-connected octahedral nodes, 8-connected cubic nodes, 6-connected hexagonal nodes, *etc.* Theoretically, the combination of Zr_6 clusters with tetracarboxylate linkers will give rise to 4,8-connected **scu**, 4,8-connected **csq**, and 4,6-connected **she** topology, depending on the connectivity of Zr_6 clusters and the conformation of tetracarboxylate linkers. Previous studies have demonstrated that the framework topology can be controlled through conformational tuning of the tetracarboxylate linkers by introducing bulky functional groups.[56] For TTF-based linkers, the substituents on the 3-position of the phenyl rings

will affect the dihedral angle between the TTF and the phenyl carboxylate plane. A smaller dihedral angle favors the **scu** network whereas a larger angle promotes the formation of a **she** network. Based on the known TTFTB, a new linker with methyl-substituents on the 3-position of the phenyl rings was designed, namely Me-TTFTB (Fig. 1a and S1†). As expected, the reaction of Zr^{4+} with TTFTB and Me-TTFTB give rise to two MOFs exhibiting **scu** and **she** topology, compounds **1** and **2**, respectively.

Compound **1** was obtained as needle-shaped microcrystals with an average size of $3 \times 1 \times 0.5$ μm. The structure of compound **1** was determined by Rietveld refinement against PXRD patterns (Table S1 and Fig. S2†). It crystalizes in the orthorhombic space group *Cmmm*, similar to the structures of previously reported NU-901 [57] and PCN-606.[58] The Zr_6 cluster in
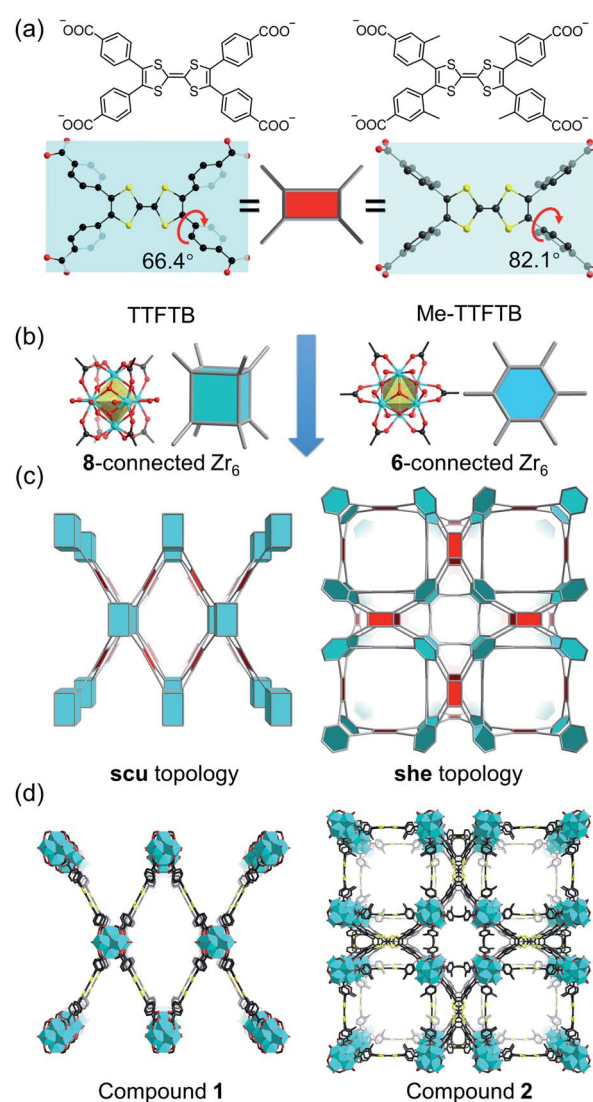

Fig. 1 Topologically guided steric tuning strategy for MOF design (a) TTFTB and Me-TTFTB linkers with different conformations. (b) 8-connected and 6-connected Zr_6 clusters. (c) Targeted topologies formed by Zr_6 clusters and conformationally differing linkers. (d) Crystal structures of compounds **1** and **2**. Color scheme: Zr, cyan; O, red; C, black; S, yellow.

compound **1** is 8-connected (Fig. 1b), therefore the overall structure can be simplified into a 4,8-connected net with **scu** topology (Fig. 1c and d). It possesses uniform channels along the *b*-axis direction with a diameter of 13.7 Å according to the crystal structure (Fig. S3 and S4†).

Single crystals of compound **2** were successfully obtained. Single crystal X-ray diffraction (SC-XRD) analysis reveals that compound **2** crystallizes in the cubic space group *Pm̄3m* (Table S2†). The asymmetric unit contains one Zr^{4+} ion, a quarter of a Me-TTFTB linker, two thirds of an O^{2-} ion, two thirds of an OH^- ion and one terminal carboxylate anion (Fig. S5†). The TTF unit is two-fold disordered with an average central $C=C$ bond length of 1.28 (3) Å (Fig. 3a), comparable to the neutral TTF moiety.[28,33,59] Each Zr_6 cluster is connected to six carboxylates from Me-TTFTB, leaving the other six sites terminated by carboxylate anions (Fig. S6†). The terminal carboxylate anions capping on the Zr_6 clusters cannot be precisely refined because of the disorder, but they were determined to be benzoate anion ($PhCOO^-$) by ^1H-NMR spectra of digested samples (Fig. S7†). The overall framework can be simplified into **she** topology if regarding the $[Zr_6O_4(OH)_4(PhCOO)_6(COO)_6]$ clusters as 6-connected hexagonal nodes and Me-TTFTB as 4-connected planar nodes (Fig. 1c). This topology is identical to PCN-224,[60] a Zr-MOF based on tetratopic porphyrin-based linkers. The topological analysis can be different when TTFTB and Me-TTFTB were regarded as two 3-connected nodes (Fig. S8†). Compound **2** shows a hierarchically porous structure with a tetragonal cage and two cubic cages (Fig. 1d and S9†). The large cubic cages are closely packed forming an interconnected channel along the *a*, *b* and *c*-direction.

The different framework structures of compounds **1** and **2** are attributed to the steric effects of the methyl groups, which force the phenyl rings to rotate off the TTF plane. Indeed, the dihedral angle between the TTF and phenyl carboxylate motif were measured to be 66.4° in compound **1** and 82.1° in compound **2** (Fig. 1a). The single crystal structure of the TTFTB linker terminated by ethoxy groups (*i.e.* TTFTB-OEt, Tables S3 and S4†) was obtained to show the dihedral angle between the TTF and phenyl carboxylate motif in small molecules. The angle in TTFTB-OEt crystals were measured to be 68.2°, which matches well with the structure of compound **1** (Fig. S1†). The steric effects of the methyl groups increase the dihedral angle and thus favor the formation of compound **2**.

Stability and porosity

The phase purity of compounds **1** and **2** bulk samples was confirmed by matching the PXRD patterns with simulations based on structural models (Fig. 2a and d). The PXRD patterns of compounds **1** and **2** are unaltered in conventional organic solvents and aqueous solution of various pH (1–12) after 24 hours' exposure (10 mg of MOF per mL of solvent), demonstrating good chemical stability (Fig. S10–S14†). N_2 adsorption isotherms also indicate that compound **2** remains porous after pH 1 and 12 treatment, although a slight decrease in total N_2 uptake was observed (Fig. S12†). TGA curves of compounds **1** and **2** under N_2 atmosphere show good thermal stability until 400 °C (Fig. S15†). To assess the porosity and surface area of compounds **1** and **2**, the N_2 sorption measurements were conducted at 77 K. Compound **1** shows a type-I isotherm with a total uptake of 393 cm^3 g^{-1} and a BET surface area of 1353 m^2 g^{-1}, indicative of a typical microporous structure (Fig. 2b). Pore size distribution derived from the adsorption isotherms shows a uniform pore size at around 12.7 Å, matching well with the structural model
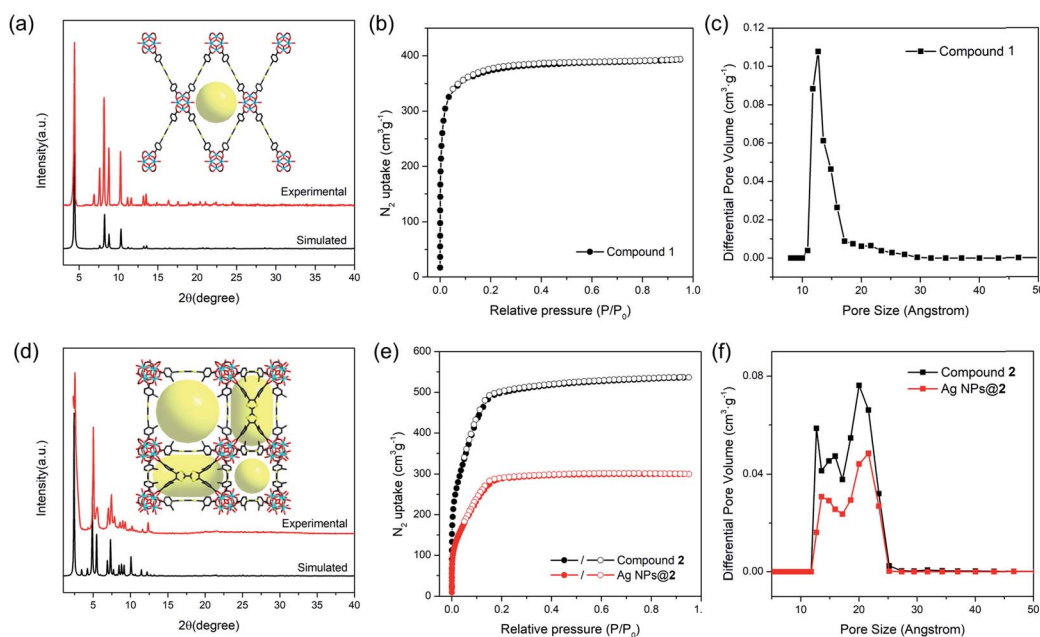

Fig. 2 The experimental and simulated PXRD patterns for compounds **1** (a) and **2** (d) after solvent removal. The N_2 adsorption–desorption isotherms of compounds **1** (b), **2** and Ag NPs@**2** (e) at 77 K. Pore size distribution of compounds **1** (c), **2** and Ag NPs@**2** (f) calculated from N_2 adsorption isotherms using a density functional theory (DFT) model.

(Fig. 2c). In contrast, type-IV isotherms were observed for compound **2** (Fig. 2e). The total N_2 uptake and BET surface area reaches 536 cm^3 g^{-1} and 1932 m^2 g^{-1} for compound **2**. Pore size distribution indicates a hierarchically porous structure with two types of micropores at 12.6 and 15.8 Å, and a mesopore of 20.7 Å (Fig. 2f), corresponding to the small cubic cages, tetragonal cages, and large cubic cages observed in single crystal structures.

Probing redox activity of compounds 1 and 2

Cyclic voltammetry (CV) of TTF-based linker, Me-H$_4$TTFTB, showed the expected redox process of TTF with two one-electron oxidation waves. The redox peaks centered at $E_{1/2} = 0.16$ and 0.38 V (vs. Fc/Fc$^+$) for Me-H$_4$TTFTB can be assigned to the TTF/TTF$^{•+}$ and TTF$^{•+}$/TTF^{2+} redox couples (Fig. S16†), which is comparable to that of H$_4$TTFTB ($E_{1/2} = 0.07$ and 0.30 V vs. Fc/Fc$^+$).[61] CV curves of compounds **1** and **2** also showed the expected redox process of TTF with two one-electron oxidation waves. The redox center was observed at $E_{1/2} = 0.40$ and 0.93 V (vs. Fc/Fc$^+$) for compound **1** and $E_{1/2} = 0.03$ and 0.96 V (vs. Fc/Fc$^+$) for compound **2**, respectively (Fig. S17–S22†). The redox activity of compound **2** was further revealed by the I$_2$ treatment. After incubating compound **2** in the I$_2$ solution in cyclohexane, an obvious color change from orange to black was observed, which can be attributed to the formation of TTF$^{•+}$ and the adsorption of I$_3^-$ species (Fig. S23†). In the crystal structure of oxidized compound **2** (namely I$_3^-$@**2**), I$_3^-$ was clearly observed as a product of the oxidation reaction (Fig. 3e and S24†). The central C–C distance increased to 1.401 (8) Å (Fig. 3b), corresponding to the conversion of double bonds in neutral TTF to single bonds in the radical cationic state TTF$^{•+}$.
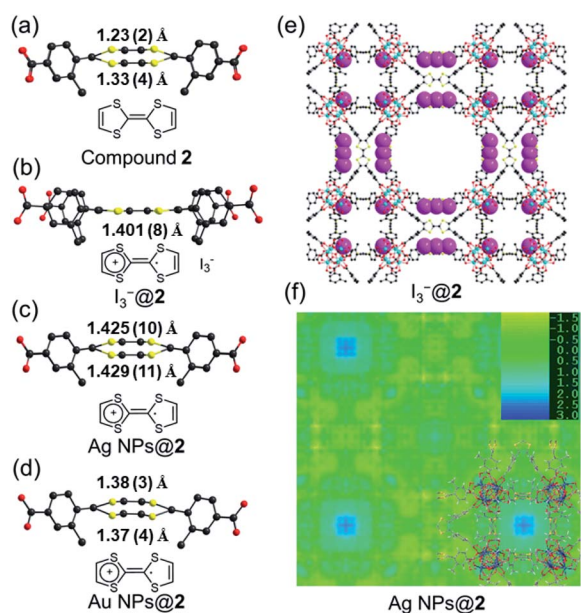
The maintained crystallinity after oxidation was also confirmed by PXRD patterns of bulk I$_3^-$@**2** samples (Fig. S25†). The incorporation of I$_3^-$ was further confirmed by IR and TGA (Fig. S26–S27†). The coordination environment and oxidation state of Zr are not affected by oxidation, as confirmed by X-ray photoelectron spectroscopy (XPS) (Fig. S28†). Electron paramagnetic resonance (EPR) studies were performed at 110 K to confirm the generation of the TTF$^{•+}$ radical (Fig. S29†). The EPR spectra showed $g = 2.002$ for I$_3^-$@**2**, matching well with those of typical TTF$^{•+}$ cation radicals.[28,62–64] Compound **1** shows redox behavior similar to compound **2** and the generation of the TTF$^{•+}$ radical upon I$_2$ treatment was confirmed by the EPR study (Fig. S30†). The foregoing results unambiguously confirm the redox activity of the TTF motif in compounds **1** and **2**.

In situ generation of metal nanoparticles

Inspired by their redox activity, we propose that the redox reaction between noble metal ions (Ag$^+$, Pd^{2+}, and Au^{3+}) and TTF-moieties will generate ultra-small metal nanoparticles in MOFs. The sulfur-rich pore environment the MOF will act as a support to stabilize the *in situ* generated nanoparticles from aggregation through a confinement effect which was also reported by Pardo and coworkers.[65] The solution of Me-H$_4$-TTFTB linker can react with the methanol solution of Ag$^+$, Pd^{2+}, and Au^{3+}, as indicated by the color change (Fig. S31†). Since the TTF moieties are well-separated within the MOF lattice, the aggregation of MNPs can be minimized.

The loading of metal-nanoparticles was realized by soaking crystals of compound **2** in a solution of AgNO$_3$, PdCl$_2$ or KAuCl$_4$, respectively. The resulting products, namely Ag NPs@**2**, Pd NPs@**2**, and Au NPs@**2**, exhibit different shades of green under an optical microscope, indicative of the generation of MNPs and TTF$^{•+}$ (Fig. 4a and S32†). High resolution transmission electron microscopy (HRTEM) images show the uniformly distributed MNPs throughout the MOF matrix. A narrow size distribution was observed with a peak at 1.6 nm for all three samples (*i.e.* Ag,
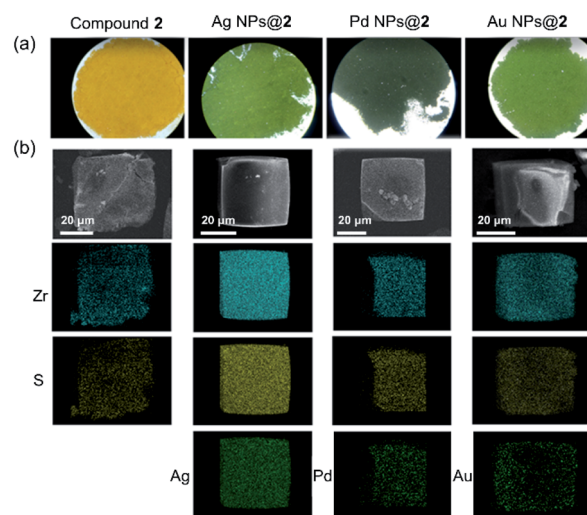

Fig. 3 The conformation of Me-TTFTB in the single crystal structure of **2** (a), I$_3^-$@**2** (b), Ag NPs@**2** (c) and Au NPs@**2** (d); (e) I$_3^-$ locations in the single crystal structure I$_3^-$@**2**. (f) Electron density map for Ag NPs@**2** single crystal structure showing strong residual electron density in the small cavity.

Fig. 4 Optical microscope images (a), and element mapping of Ag NPs@**2**, Pd NPs@**2**, and Au NPs@**2** under SEM/EDX (b).

Pd, and Au), in line with the size of the framework's small cavity (Fig. S33†). Note that the calculated average sizes of NPs might be overestimated because of nanoparticle overlap in the TEM images. The distance between lattice fringes were measured to be 0.236, 0.243, and 0.245 nm for Ag, Pd, and Au, corresponding to the spacing of (111),[66] 1/3(422) (face-centered cubic Pd),[67] and (111)[66] lattice planes (Fig. 5). The noble metal species were uniformly distributed throughout the MOF particle, as indicated by elemental mapping under a scanning electron microscope with energy-dispersive X-ray spectroscopy (SEM/EDX) (Fig. 4b and S34–S36†).

The position of MNPs within the MOF structures were investigated by single crystal synchrotron X-ray diffraction study and N_2 adsorption isotherms. The single crystal structure of Ag NPs@2 (Table S5†) shows a strong electron density at the center of the cubic cavity, which is attributed to the Ag NPs (Fig. 3f). An elongated C–C bond distance (1.427 (10) Å) was observed in TTF moieties, corresponding to the partial oxidation of TTF into TTF$^{•+}$ radicals by Ag$^+$ (Fig. 3c). Similar behavior was also observed in Au NPs@2 with an average C–C bond distance of 1.38 (3) Å (Fig. 3d and S37†). Meanwhile, the reduced C–S distance of Ag NPs@2 (1.676 (7) Å) and Au NPs@2 (1.690 (8) Å) compared to the original compound 2 (1.773 (7) Å), also suggested the partial oxidation of the TTF (Table S7†).[68] Furthermore, pore size distributions derived from N_2 adsorption isotherms show a significant reduction in the amount of 12.6 Å micropores while the larger pores at 15.6 and 21.4 Å are maintained (Fig. 2f). These results imply that Ag NPs occupy the small cavities.

The crystallinity of compound 2 after metal nanoparticle (MNP) loading was confirmed by PXRD studies (Fig. S25 and S38†). The diffraction peaks of MNPs are not observed due to their small size.[14,15,20] The total metal loadings of Ag, Pd, and Au in compound 2 were determined to be 3.4 wt%, 3.4 wt%, and 4.2 wt%, respectively, by inductively coupled plasma atomic emission spectroscopy (ICP-AES, Table S7†). X-ray photoelectron spectroscopy (XPS) further revealed that all the Ag within Ag NPs@2 exist as Ag^0 whereas only half of the Pd and Au species exist as Pd^0 and Au^0 (Fig. S39–S42†). The Pd^{2+} and Au^{3+} were attributed to the metal salts trapped in the MOF cavity.
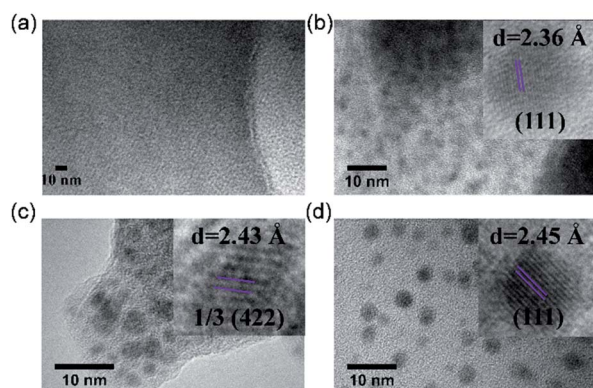
Therefore, the loadings of MNPs (excluding metal cations) were calculated to be 3.4 wt%, 1.7 wt%, and 2.2 wt% for Ag, Pd, and Au. Accordingly, they are formulated as Ag$^0_{0.75}$[Zr$_6$(Me-TTFTB)$_{1.5}$O$_4$(OH)$_4$(C$_6$H$_5$COO)$_6$]·(NO$_3$)$_{0.75}$, Pd$^0_{0.38}$Pd$^{2+}_{0.38}$[Zr$_6$(Me-TTFTB)$_{1.5}$O$_4$(OH)$_4$(C$_6$H$_5$COO)$_6$]·Cl$_{1.5}$, and Au$^0_{0.25}$Au$^{3+}_{0.25}$[Zr$_6$(Me-TTFTB)$_{1.5}$O$_4$(OH)$_4$(C$_6$H$_5$COO)$_6$]·Cl$_{1.5}$. Based on the loading of MNPs, about half of the TTF molecules was oxidized by Ag$^+$, Pd^{2+}, and Au^{3+} within compound 2. EPR studies of MNPs@2 samples at 110 K further confirm the formation of TTF$^{•+}$ radicals (Fig. S43–S45†). Notably, the anisotropic signal of MNPs@2 as well as MNPs@1 (Fig. S30†) can be originated from the hyperfine coupling of sulfur and carbon atoms in the TTF molecule which exist in all the samples. Owing to the overlap of multiple peaks, this hyperfine coupling was not obvious in some samples such as Ag NPs@2 and Au NPs@2. To balance the charge, Ag NPs@2 includes free NO$_3^-$ ions as revealed by the unsplit 1382 cm^{-1} peak in the IR spectra (Fig. S46†);[14,15,20] Pd NPs@2 and Au NPs@2 include free Cl$^-$ ions as indicated by the SEM-EDX (Fig. S35 and S36†).

Following a similar synthetic procedure, MNPs can also be loaded into compound 1. The successful synthesis of MNPs@1 (M = Ag, Pd, and Au) was evidenced by optical images (Fig. S47†), PXRD (Fig. S48†), TGA (Fig. S49†), XPS (Fig. S50–S54†), SEM/EDX (Fig. S55–S61†), and TEM (Fig. S62–S64†). The total metal loadings were determined to be 4.6 wt%, 4.5 wt%, and 5.5 wt% for Ag, Pd, and Au by ICP-AES.

Compared to the traditional syntheses of MNPs@MOF materials, the presented redox-active MOF systems offer facile control of nanoparticle sizes. Ultra-small nanoparticles (<2 nm) with uniform sizes can be easily obtained under a wide range of synthetic conditions. Similar concept has been demonstrated by Pardo et al.[69] For comparison, the size of nanoparticles synthesized by external reductants are highly sensitive to the concentration of reductant and metal ions, temperature, and reaction time. Furthermore, the hierarchically porous structure of compound 2 allows for the immobilization of MNPs within the small cavity, leaving the large mesopores and interconnected channels open for the diffusion of metal salts/substrates.

Aerobic oxidation of alcohols by Pd NPs@2

Ultra-small metal nanoparticles immobilized in a stable and hierarchically porous framework afford an ideal platform for heterogeneous catalysis. As a proof of concept, Pd NPs@2 was selected as a catalyst for aerobic alcohol oxidation (Fig. S65†), a reaction widely used in organic synthesis and chemical industry. The oxidation reaction of benzyl alcohol was carried out with Pd NPs@2 under 0.1 MPa O$_2$ at 90 °C in cyclohexane. Pd NPs@2 shows good activity with nearly 100% conversion and more than 50% selectivity toward benzaldehyde (Table S8†). A broad substrate scope of substrates bearing electron-rich and electron-deficient functional groups were converted to corresponding aldehyde in good yields (Table S9†). Control experiments using compound 2 without Pd NPs do not show any activity, suggesting Pd NPs to be the active sites (Fig. S66, S67 and Table S10†). To confirm the heterogeneous nature of catalysis, hot filtration was carried out by removing the MOF catalysts from

Fig. 5 HRTEM images of 2 (a), Ag NPs@2 (b), Pd NPs@2 (c), and Au NPs@2 (d).

the reaction mixture, after which no further reaction was observed (Fig. S66†). As a heterogeneous catalyst, Pd NPs@2 can be easily recycled from the reaction system by centrifugation and reused in successive runs. Recycling experiments demonstrated that the Pd NPs@2 catalyst can be reused three times without significant loss of conversion and selectivity (Fig. S68 and Table S8†). Considering the large pore size of compound 2 and diverse metal species that can be incorporated, a wide range of catalytic reactions can be envisioned in this MOF system.

Conclusions

In conclusion, we designed two stable and redox-active MOFs incorporating robust Zr_6 clusters and redox-active TTF-based linkers. Among them, compound 2 shows hierarchical porosity with both microporous and mesoporous cages. Taking advantage of the stable framework and redox-active TTF-moieties, noble metal (Ag, Pd, and Au) nanoparticles can be generated in situ and stabilized in the MOF cavity by the reduction of respective metal cations. Single crystal structures, TEM images, and pore size distributions derived from N_2 adsorption measurements indicate ultra-small metal nanoparticles located in the microporous cavity, leaving the larger cages open for guest diffusion. A heterogeneous catalyst for aerobic oxidation of alcohols was synthesized by incorporating Pd nanoparticles in compound 2. The high chemical stability, hierarchical porosity, and redox activity of the MOF matrices promise future applications in heterogeneous catalysis and beyond. Further research activities are undergoing to enrich the structures and compositions of the MNPs@redox-MOF systems and to extend their applications into the field of conductive porous materials and electrocatalysis.

Experimental section

Synthesis of compound H₄TTFTB

H₄TTFTB were prepared adopting the previously reported procedure.[28]

Synthesis of compound Me-H₄TTFTB

Me-H₄TTFTB were synthesized similar to H₄TTFTB with methyl-4-bromo-3-methylbenzoate instead of ethyl-4-bromobenzoate. Me-H₄TTFTB in red solid was obtained with a yield of 36%. ^{1}H NMR (400 MHz, d₆-DMSO) δ 13.06 (br, 4H), 7.73 (s, 4H), 7.66–7.64 (d, 4H), 7.40–7.39 (d, 4H), 2.32 (s, 12H); ESI-MS m/z calcd for $C_{38}H_{28}O_8S_4$ [M − H⁻] 739.08, found 739.07. FT-IR (KBr pellet, cm⁻¹): 2971 w, 2532 w, 1692 vs., 16 606 s, 1563 m, 1417 m, 1288 vs., 1257 s, 1190 s, 1125 s, 1048 m, 903 m, 839 m, 758 s, 559 m, 445 m.

Synthesis of compound 1: [Zr₆(TTFTB)₂O₈(OH₂)₈]·2(C₃H₇ON)

To a solution of H₄TTFTB (0.010 g, 0.015 mmol) and ZrCl₄ (0.020 g, 0.086 mmol) in 3 mL DMF, benzoic acid (0.6 g, 4.91 mmol) was added. The mixture was capped and heated to 120 °C for 72 h then cooled to room temperature at a rate of 5 °C h⁻¹. Red microcrystals (0.013 g) of 1 were obtained by filtration

and washed with DMF and acetone three times. Yield 74.5% (based on H₄TTFTB). Calcd for $C_{74}H_{62}N_2O_{34}S_8Zr_6$ (Mr = 2327.14 g mol⁻¹): C, 38.19; H, 2.69; N, 1.20%. Found: C, 37.50; H, 2.83; N, 0.98%. FT-IR (KBr pellet, cm⁻¹): 3667 w, 2360 m, 1662 s, 1601 s, 1558 s, 1418 vs., 1180 m, 1101 m, 1019 m, 866 m, 807 m, 768 m, 649 s, 569 m, 471 m.

Synthesis of compound 2: [Zr₆(Me-TTFTB)₁.₅O₄(OH)₄(C₆H₅COO)₆]·20(H₂O)·4(C₃H₇ON)

To a solution of Me-H₄TTFTB (0.010 g, 0.013 mmol), ZrCl₄ (0.030 g, 0.129 mmol) and benzoic acid (0.6 g, 4.91 mmol) in 3 mL DMF was added 0.1 mL water. The mixture was capped and heated to 120 °C for 72 h, then cooled to room temperature at a rate of 5 °C h⁻¹. Orange-yellow cubic crystals (0.007 g) of 2 were obtained by filtration and washed with DMF and acetone three times. Yield 25.5% (based on Me-H₄TTFTB). Calcd for $C_{111}H_{138}N_4O_{56}S_6Zr_6$ (Mr = 3164.01 g mol⁻¹): C, 42.14; H, 4.40; N, 1.77%. Found: C, 40.06; H, 4.10; N, 1.98%. FT-IR (KBr pellet, cm⁻¹): 3421 w, 1653 s, 1598 s, 1544 vs., 1419 vs., 1243 m, 1028 m, 777 m, 721 s, 644 m, 460 m.

Synthesis of compound I₃⁻@1: [Zr₆(TTFTB)₂O₈(OH₂)₈]·(I₃)₂·8(C₆H₁₂)

Iodine oxidation to produce I₃⁻@1 was undertaken using a solid-solution diffusion technique. Crystals of 1 were soaked in 0.1 M iodine in cyclohexane solution for 12 hours at room temperature. Over time, the crystals' color deepened until becoming black. The obtained crystals were washed by cyclohexane three times. The quantities of iodine incorporated were confirmed by TGA (Fig. S39†) and elemental analysis: two I₃⁻ for I₃⁻@1 per unit cell. Anal. Calcd. For $C_{116}H_{144}O_{32}S_8Zr_6I_6$ (Mr = 3615.66 g mol⁻¹): C, 38.53; H, 4.01%. Found: C, 36.24; H, 3.35%. Selected IR data (KBr, cm⁻¹): 3423 w, 2362 w, 1604 s, 1543 s, 1420 vs., 1285 w, 1185 m, 1144 w, 1108w, 1017 m, 865 w, 809 m, 768 w, 704 w, 654 s, 568 w, 465 m.

Synthesis of compound I₃⁻@2: [Zr₆(Me-TTFTB)₁.₅O₄(OH)₄(C₆H₅COO)₆]·(I₃)₁.₅·1.5(C₆H₁₂)

The iodine oxidation of I₃⁻@2 was undertaken using a solid-solution diffusion technique. Crystals of 2 were soaked in 0.1 M iodine in cyclohexane solution for 12 hours at room temperature. The color of crystals changed from orange to black. The obtained crystals were washed by cyclohexane for three times. The quantities of iodine incorporated were confirmed by TGA (Fig. S16†) and elemental analysis: a quarter of I₃⁻ for I₃⁻@2 per unit cell. Anal. Calcd. For $C_{108}H_{88}O_{32}S_6Zr_6I_{4.5}$ (Mr = 3208.64 g mol⁻¹): C, 40.43; H, 2.76%. Found: C, 38.89; H, 2.31%. Selected IR data (KBr, cm⁻¹): 3344 w, 2921 m, 1598 s, 1550 s, 1491 w, 1421 vs., 842 w, 777 m, 721 s, 651 s, 489 w, 461 m, 407 w.

Synthesis of MNPs@1 and MNPs@2 (M = Ag, Pd, and Au)

Crystals of compound 1 were immersed in 0.1 mol L⁻¹ AgNO₃, PdCl₂ or KAuCl₄ methanol solutions for 24 h in the dark. The color of crystals changed from orange to black. The obtained products were washed by fresh methanol for three times to

remove the metal salts. Ag NPs@**1**: $Ag^0[Zr_6(TTFTB)_2O_8(OH_2)_8]$·$(NO_3)$; Pd NPs@**1**: $Pd^0_{0.5}Pd^{2+}_{0.5}[Zr_6(TTFTB)_2O_8(OH_2)_8]$·$Cl_2$; Au NPs@**1**: $Au^0_{0.33}Au^{3+}_{0.33}[Zr_6(TTFTB)_2O_8(OH_2)_8]$·$Cl_2$. MNPs@**2** were synthesized by a similar method except that compound **2** were used. Ag NPs@**2**: $Ag^0_{0.75}[Zr_6(Me\text{-}TTFTB)_{1.5}O_4(OH)_4(C_6H_5COO)_6]$·$(NO_3)_{0.75}$; Pd NPs@**2**: $Pd^0_{0.38}Pd^{2+}_{0.38}[Zr_6(Me\text{-}TTFTB)_{1.5}O_4(OH)_4(C_6H_5COO)_6]$·$Cl_{1.5}$; Au NPs@**2**: $Au^0_{0.25}Au^{3+}_{0.25}[Zr_6(Me\text{-}TTFTB)_{1.5}O_4(OH)_4(C_6H_5COO)_6]$·$Cl_{1.5}$.

Conflicts of interest

There are no conflicts to declare.

Acknowledgements

Notes and references

1 H. C. Zhou, J. R. Long and O. M. Yaghi, *Chem. Rev.*, 2012, **112**, 673–674.

2 J. R. Li, R. J. Kuppler and H. C. Zhou, *Chem. Soc. Rev.*, 2009, **38**, 1477–1504.

3 J. R. Li, J. Sculley and H. C. Zhou, *Chem. Rev.*, 2012, **112**, 869–932.

4 W. Zhao, J. Peng, W. Wang, S. Liu, Q. Zhao and W. Huang, *Coord. Chem. Rev.*, 2018, **377**, 44–63.

5 J. Lee, O. K. Farha, J. Roberts, K. A. Scheidt, S. T. Nguyen and J. T. Hupp, *Chem. Soc. Rev.*, 2009, **38**, 1450–1459.

6 I. Stassen, N. Burtch, A. Talin, P. Falcaro, M. Allendorf and R. Ameloot, *Chem. Soc. Rev.*, 2017, **46**, 3185–3241.

7 M. L. Aubrey, B. M. Wiers, S. C. Andrews, T. Sakurai, S. E. Reyes-Lillo, S. M. Hamed, C. J. Yu, L. E. Darago, J. A. Mason, J. O. Baeg, F. Grandjean, G. J. Long, S. Seki, J. B. Neaton, P. Yang and J. R. Long, *Nat. Mater.*, 2018, **17**, 625–632.

8 H. J. Choi and M. P. Suh, *J. Am. Chem. Soc.*, 2004, **126**, 15844–15851.

9 G. Férey, F. Millange, M. Morcrette, C. Serre, M.-L. Doublet, J.-M. Grenèche and J.-M. Tarascon, *Angew. Chem.*, 2007, **119**, 3323–3327.

10 H. R. Moon, J. H. Kim and M. P. Suh, *Angew. Chem., Int. Ed.*, 2005, **44**, 1261–1265.

11 B. Tu, Q. Pang, H. Xu, X. Li, Y. Wang, Z. Ma, L. Weng and Q. Li, *J. Am. Chem. Soc.*, 2017, **139**, 7998–8007.

12 Y. Tulchinsky, C. H. Hendon, K. A. Lomachenko, E. Borfecchia, B. C. Melot, M. R. Hudson, J. D. Tarver, M. D. Korzynski, A. W. Stubbs, J. J. Kagan, C. Lamberti, C. M. Brown and M. Dinca, *J. Am. Chem. Soc.*, 2017, **139**, 5992–5997.

13 Y. M. Litvinova, Y. M. Gayfulin, K. A. Kovalenko, D. G. Samsonenko, J. van Leusen, I. V. Korolkov, V. P. Fedin and Y. V. Mironov, *Inorg. Chem.*, 2018, **57**, 2072–2084.

14 M. P. Suh, H. R. Moon, E. Y. Lee and S. Y. Jang, *J. Am. Chem. Soc.*, 2006, **128**, 4710–4718.

15 Y. E. Cheon and M. P. Suh, *Chem.–Eur. J.*, 2008, **14**, 3961–3967.

16 S. S. Park, E. R. Hontz, L. Sun, C. H. Hendon, A. Walsh, T. Van Voorhis and M. Dinca, *J. Am. Chem. Soc.*, 2015, **137**, 1774–1777.

17 T. C. Narayan, T. Miyakai, S. Seki and M. Dinca, *J. Am. Chem. Soc.*, 2012, **134**, 12932–12935.

18 Q. Chen, J. Sun, P. Li, I. Hod, P. Z. Moghadam, Z. S. Kean, R. Q. Snurr, J. T. Hupp, O. K. Farha and J. F. Stoddart, *J. Am. Chem. Soc.*, 2016, **138**, 14242–14245.

19 R. Murase, B. F. Abrahams, D. M. D'Alessandro, C. G. Davies, T. A. Hudson, G. N. L. Jameson, B. Moubaraki, K. S. Murray, R. Robson and A. L. Sutton, *Inorg. Chem.*, 2017, **56**, 9025–9035.

20 Y. E. Cheon and M. P. Suh, *Angew. Chem., Int. Ed.*, 2009, **48**, 2899–2903.

21 A. F. Cozzolino, C. K. Brozek, R. D. Palmer, J. Yano, M. Li and M. Dinca, *J. Am. Chem. Soc.*, 2014, **136**, 3334–3337.

22 J. Y. Ha, J. Y. Koo, H. Ohtsu, Y. Yakiyama, K. Kim, D. Hashizume and M. Kawano, *Angew. Chem., Int. Ed.*, 2018, **57**, 4717–4721.

23 B. A. Johnson, A. Bhunia, H. Fei, S. M. Cohen and S. Ott, *J. Am. Chem. Soc.*, 2018, **140**, 2985–2994.

24 M. E. Ziebel, L. E. Darago and J. R. Long, *J. Am. Chem. Soc.*, 2018, **140**, 3040–3051.

25 I. Hod, W. Bury, D. M. Gardner, P. Deria, V. Roznyatovskiy, M. R. Wasielewski, O. K. Farha and J. T. Hupp, *J. Phys. Chem. Lett.*, 2015, **6**, 586–591.

26 A. Van Wyk, T. Smith, J. Park and P. Deria, *J. Am. Chem. Soc.*, 2018, **140**, 2756–2760.

27 D. M. D'Alessandro, *Chem. Commun.*, 2016, **52**, 8957–8971.

28 J. Su, S. Yuan, H. Y. Wang, L. Huang, J. Y. Ge, E. Joseph, J. Qin, T. Cagin, J. L. Zuo and H. C. Zhou, *Nat. Commun.*, 2017, **8**, 2008.

29 M. Souto, J. Romero, J. Calbo, I. J. Vitorica-Yrezabal, J. L. Zafra, J. Casado, E. Orti, A. Walsh and G. Minguez Espallargas, *J. Am. Chem. Soc.*, 2018, **140**, 10562–10569.

30 M. Souto, A. Santiago-Portillo, M. Palomino, I. J. Vitorica-Yrezabal, B. J. C. Vieira, J. C. Waerenborgh, S. Valencia, S. Navalon, F. Rey, H. Garcia and G. Minguez Espallargas, *Chem. Sci.*, 2018, **9**, 2413–2418.

31 K. S. Pedersen, P. Perlepe, M. L. Aubrey, D. N. Woodruff, S. E. Reyes-Lillo, A. Reinholdt, L. Voigt, Z. Li, K. Borup, M. Rouzieres, D. Samohvalov, F. Wilhelm, A. Rogalev, J. B. Neaton, J. R. Long and R. Clerac, *Nat. Chem.*, 2018, **10**, 1056–1061.

32 F. Pointillart, B. le Guennic, O. Cador, O. Maury and L. Ouahab, *Acc. Chem. Res.*, 2015, **48**, 2834–2842.

33 H. Y. Wang, J. Y. Ge, C. Hua, C. Q. Jiao, Y. Wu, C. F. Leong, D. M. D'Alessandro, T. Liu and J. L. Zuo, *Angew. Chem., Int. Ed.*, 2017, **56**, 5465–5470.

34 H. Wang, Q.-L. Zhu, R. Zou and Q. Xu, *Chem*, 2017, **2**, 52–80.

35 Y. Zhang, S. N. Riduan and J. Wang, *Chem.–Eur. J.*, 2017, **23**, 16419–16431.

36 H. B. Wu and X. W. D. Lou, *Sci. Adv.*, 2017, **3**, eaap9252.

37 P. M. Usov, C. Fabian and D. M. D'Alessandro, *Chem. Commun.*, 2012, **48**, 3945–3947.

38 Z. Zhang, H. Yoshikawa and K. Awaga, *J. Am. Chem. Soc.*, 2014, **136**, 16112–16115.

39 Y. Wang, W. Zhu, W. Du, X. Liu, X. Zhang, H. Dong and W. Hu, *Angew. Chem., Int. Ed.*, 2018, **57**, 3963–3967.

40 J. S. Park, J. Park, Y. J. Yang, T. T. Tran, I. S. Kim and J. L. Sessler, *J. Am. Chem. Soc.*, 2018, **140**, 7598–7604.

41 J. Ferraris, D. O. Cowan, V. Walatka and J. H. Perlstein, *J. Am. Chem. Soc.*, 1973, **95**, 948–949.

42 E. Coronado, J. R. Galan-Mascaros, C. J. Gomez-Garcia and V. Laukhin, *Nature*, 2000, **408**, 447–449.

43 T. Enoki and A. Miyazaki, *Chem. Rev.*, 2004, **104**, 5449–5478.

44 C. Rovira, *Chem. Rev.*, 2004, **104**, 5289–5318.

45 R. P. Shibaeva and E. B. Yagubskii, *Chem. Rev.*, 2004, **104**, 5347–5378.

46 S. S. Park, A. J. Rieth, C. H. Hendon and M. Dinca, *J. Am. Chem. Soc.*, 2018, **140**, 2016–2019.

47 S. S. Park, C. H. Hendon, A. J. Fielding, A. Walsh, M. O'Keeffe and M. Dinca, *J. Am. Chem. Soc.*, 2017, **139**, 3619–3622.

48 L. Sun, M. G. Campbell and M. Dinca, *Angew. Chem., Int. Ed.*, 2016, **55**, 3566–3579.

49 L. S. Xie, E. V. Alexandrov, G. Skorupskii, D. M. Proserpio and M. Dinca, *Chem. Sci.*, 2019, **10**, 8558–8565.

50 Q.-L. Zhu and Q. Xu, *Chem*, 2016, **1**, 220–245.

51 S. Dang, Q.-L. Zhu and Q. Xu, *Nat. Rev. Mater.*, 2017, **3**, 17075.

52 Z. Li and Q. Xu, *Acc. Chem. Res.*, 2017, **50**, 1449–1458.

53 Q. Yang, Q. Xu and H.-L. Jiang, *Chem. Soc. Rev.*, 2017, **46**, 4774–4808.

54 H. R. Moon and M. P. Suh, *Eur. J. Inorg. Chem.*, 2010, **2010**, 3795–3803.

55 S. Yuan, L. Feng, K. Wang, J. Pang, M. Bosch, C. Lollar, Y. Sun, J. Qin, X. Yang, P. Zhang, Q. Wang, L. Zou, Y. Zhang, L. Zhang, Y. Fang, J. Li and H. C. Zhou, *Adv. Mater.*, 2018, **30**, e1704303.

56 J. Pang, S. Yuan, J. Qin, C. Liu, C. Lollar, M. Wu, D. Yuan, H. C. Zhou and M. Hong, *J. Am. Chem. Soc.*, 2017, **139**, 16939–16945.

57 C.-W. Kung, T. C. Wang, J. E. Mondloch, D. Fairen-Jimenez, D. M. Gardner, W. Bury, J. M. Klingsporn, J. C. Barnes, R. Van Duyne, J. F. Stoddart, M. R. Wasielewski, O. K. Farha and J. T. Hupp, *Chem. Mater.*, 2013, **25**, 5012–5017.

58 J. Pang, S. Yuan, D. Du, C. Lollar, L. Zhang, M. Wu, D. Yuan, H. C. Zhou and M. Hong, *Angew. Chem., Int. Ed.*, 2017, **56**, 14622–14626.

59 J. Su, T. H. Hu, R. Murase, H. Y. Wang, D. M. D'Alessandro, M. Kurmoo and J. L. Zuo, *Inorg. Chem.*, 2019, **58**, 3698–3706.

60 D. Feng, W. C. Chung, Z. Wei, Z. Y. Gu, H. L. Jiang, Y. P. Chen, D. J. Darensbourg and H. C. Zhou, *J. Am. Chem. Soc.*, 2013, **135**, 17105–17110.

61 C. F. Leong, C.-H. Wang, C. D. Ling and D. M. D'Alessandro, *Polyhedron*, 2018, **154**, 334–342.

62 R. Berridge, P. J. Skabara, C. Pozo-Gonzalo, A. Kanibolotsky, J. Lohr, J. J. McDouall, E. J. McInnes, J. Wolowska, C. Winder, N. S. Sariciftci, R. W. Harrington and W. Clegg, *J. Phys. Chem. B*, 2006, **110**, 3140–3152.

63 E. Gomar-Nadal, L. Mugica, J. Vidal-Gancedo, J. Casado, J. T. L. Navarrete, J. Veciana, C. Rovira and D. B. Amabilino, *Macromolecules*, 2007, **40**, 7521–7531.

64 H.-Y. Wang, L. Cui, J.-Z. Xie, C. F. Leong, D. M. D'Alessandro and J.-L. Zuo, *Coord. Chem. Rev.*, 2017, **345**, 342–361.

65 M. Mon, M. A. Rivero-Crespo, J. Ferrando-Soria, A. Vidal-Moya, M. Boronat, A. Leyva-Perez, A. Corma, J. C. Hernandez-Garrido, M. Lopez-Haro, J. J. Calvino, G. Ragazzon, A. Credi, D. Armentano and E. Pardo, *Angew. Chem., Int. Ed.*, 2018, **57**, 6186–6191.

66 Y. Wei, S. Han, D. A. Walker, P. E. Fuller and B. A. Grzybowski, *Angew. Chem., Int. Ed.*, 2012, **51**, 7435–7439.

67 X. Huang, S. Tang, J. Yang, Y. Tan and N. Zheng, *J. Am. Chem. Soc.*, 2011, **133**, 15946–15949.

68 F. Pointillart, Y. Le Gal, S. Golhen, O. Cador and L. Ouahab, *Chem. Commun.*, 2009, 3777–3779, DOI: 10.1039/b901932d.

69 F. R. Fortea-Perez, M. Mon, J. Ferrando-Soria, M. Boronat, A. Leyva-Perez, A. Corma, J. M. Herrera, D. Osadchii, J. Gascon, D. Armentano and E. Pardo, *Nat. Mater.*, 2017, **16**, 760–766.